

A detailed study on spectroscopic performance of SOI pixel detector with a pinned depleted diode structure for X-ray astronomy

Masataka Yukumoto^{a,*}, Koji Mori^a, Ayaki Takeda^a, Yusuke Nishioka^a, Miraku Kimura^a, Yuta Fuchita^a, Taiga Yoshida^a, Takeshi G. Tsuru^b, Ikuo Kurachi^c, Kouichi Hagino^d, Yasuo Arai^e, Takayoshi Kohmura^f, Takaaki Tanaka^g, Kumiko K. Nobukawa^h

^aDepartment of Applied Physics, Faculty of Engineering, University of Miyazaki, 1-1 Gakuen-Kibanadai-Nishi, Miyazaki, 889-2192, Japan

^bDepartment of Physics, Faculty of Science, Kyoto University, Kitashirakawa Oiwake-cho, Sakyo-ku, Kyoto 606-8502, Japan

^cD&S Inc., 774-3-213 Higashiasakawacho, Hachioji, Tokyo 193-0834, Japan

^dDepartment of Physics, University of Tokyo, 7-3-1 Hongo, Bunkyo, Tokyo 113-0033, Japan

^eAccelerator Laboratory, High Energy Accelerator Research Organization (KEK), 1-1 Oho, Tsukuba 305-0801, Japan

^fDepartment of Physics and Astronomy, Faculty of Science and Technology, Tokyo University of Science, 2641 Yamazaki, Noda, Chiba 278-8510, Japan

^gDepartment of Physics, Konan University, 8-9-1 Okamoto, Higashinada, Kobe, Hyogo 658-8501, Japan

^hFaculty of Science and Engineering, Kindai University, 3-4-1 Kowakae, Higashi-Osaka, Osaka 577-8502, Japan

Abstract

We have been developing silicon-on-insulator (SOI) pixel detectors with a pinned depleted diode (PDD) structure, named “XRPIX”, for X-ray astronomy. In our previous study, we successfully optimized the design of the PDD structure, achieving both the suppression of large leakage current and satisfactory X-ray spectroscopic performance. Here, we report a detailed study on the X-ray spectroscopic performance of the XRPIX with the optimized PDD structure. The data were obtained at $-60\text{ }^{\circ}\text{C}$ with the “event-driven readout mode”, in which only a triggering pixel and its surroundings are read out. The energy resolutions in full width at half maximum at 6.4 keV are $178 \pm 1\text{ eV}$ and $291 \pm 1\text{ eV}$ for single-pixel and all-pixel event spectra, respectively. The all-pixel events include charge-sharing pixel events as well as the single-pixel events. These values are the best achieved in the history of our development. We argue that the gain non-linearity in the low energy side due to excessive charge injection to the charge-sensitive amplifier is a major factor to limit the current spectroscopic performance. Optimization of the amount of the charge injection is expected to lead to further improvement in the spectroscopic performance of XRPIX, especially for the all-pixel event spectrum.

Keywords: X-ray detectors, X-ray SOIPIX, Monolithic active pixel sensors, Silicon on insulator technology

1. Introduction

Charge-coupled devices (CCDs) had been the most widely used image sensor both in commercial and astronomical uses for long time since its appearance. At least in commercial use, it has been a while since complementary metal-oxide-semiconductor (CMOS) sensors almost completely replaced CCDs. CMOS sensors inherently possess several advantages over CCDs such as lower power consumption, lower voltage operation, faster readout, on-chip functionality, and so on [1].

Their lower power consumption and lower voltage operation are especially beneficial in the consumer electronics market and have been the driving force behind overturning the prevalence of CCDs. A similar trend is coming in the astronomical field [2], and X-ray astronomy is also no exception. Progress in X-ray astronomy over the last three decades undoubtedly owes much to CCD detectors [3, 4, 5, 6]. The X-ray CCD detectors keep advancing and new X-ray observatories still utilize their utility and reliability [7, 8, 9, 10, 11]. Under these circumstances, X-ray CMOS detectors are certainly presenting new possibilities beyond X-ray CCDs for future X-ray astronomy. We summarize the performance of modern X-ray CCDs and CMOS detector for X-ray astronomy in Table 1

*Corresponding author

Email addresses: yukumoto@astro.miyazaki-u.ac.jp (Masataka Yukumoto), mori@astro.miyazaki-u.ac.jp (Koji Mori)

Table 1: Performance of modern X-ray CCDs and CMOS detector for X-ray astronomy.

	pnCCD [12]	fast-readout CCD for AXIS [13]	scientific CMOS for Einstein Probe [14]
Number of pixels	384 × 384	1440 × 1440	4096 × 4096
Pixel size	75 μm square	24 μm square	15 μm square
Sensor layer thickness	450 μm	100 μm	10 μm
Time resolution / Frame rate	50 msec	≤5 fps	20 fps
Energy resolution at 6 keV (Single-pixel event)	~ 133 eV at −85 °C	129 eV at −87 °C	140 eV at room temp.

One concern in applying conventional CMOS sensors for X-ray astronomy is its low quantum efficiency for X-ray. Their sensor layer thickness is typically a few μm. A thick sensor layer of >100 μm is necessary for X-ray detection up to 10 keV with high quantum efficiency. To overcome this situation, we have been developing a novel CMOS pixel detector, named “XRPIX”, based on silicon-on-insulator (SOI) CMOS technology [15]. The SOI CMOS technology allows both a thick high-resistivity silicon for sensor layer and a low-resistivity silicon for high-speed circuit to coexist in a single monolithic detector [16]. XRPIX achieves a more than 300 μm-thick fully depleted sensor layer.

Utilizing the on-chip functionality, XRPIX incorporates a self-trigger function in each pixel [17]. Restricting readout pixels to a triggering and its surroundings ones enables XRPIX to achieve a fine time resolution of ~10 μsec with a high throughput of ~1 kHz. With this “event-driven readout mode”, XRPIX can significantly reduce non-X-ray background by applying the anti-coincidence technique and mitigate the degree of event pile-up for point sources.

The event-driven readout mode of XRPIX is certainly unique function beyond X-ray CCDs. However, with regard to spectroscopic performance, XRPIX still falls behind X-ray CCDs. We have recently developed XRPIX8 to improve the spectroscopic performance of XRPIX introducing a Pinned Depleted Diode (PDD) structure in the sensor layer [18]. The PDD structure is relatively complex compared to our previous XRPIXs and optimization studies were necessary to finalize the design of the PDD structure. We successfully found out the best design, achieving both the suppression of large leakage current and satisfactory X-ray spectroscopic performance [19]. Here, we report a detailed study on the spectroscopic performance of XRPIX8 with the optimized PDD structure¹. We also provide our post data-

acquisition (DAQ) processing. The data was obtained with the event-driven readout mode at −60 °C, the lowest operation temperature of our intended use. This spectroscopic performance study was performed for not only the single-pixel events but also the all-pixel events including charge-sharing pixel events. Evaluation only with single pixel events is useful for understanding basic response of pixel detectors, especially in the early stage of the development. Actually, we have been evaluating our XRPIX with single pixel events. On the other hand, the fraction of single pixel events is typically less than half of the total, about 20 % in our case. Therefore, evaluation with all-pixel events including charge-sharing pixel events is necessary to utilize all the events detected.

Section 2 gives the device description of XRPIX8 and data format of the event-driven readout mode. Section 3 describes the post DAQ processing step by step. Section 4 presents the details of the spectroscopic performance of XRPIX8. Then, Section 5 discusses the causes limiting the current spectroscopic performance. Finally, Section 6 summarizes this study.

2. Device and data description

Table 2: Specifications of XRPIX8.

Chip size	6 mm square
Number of pixels	96 × 96
Pixel size	36 μm square
Sensor layer thickness	300 μm

The details of XRPIX8, including the PDD structure, are given in [19]. Table 2 particularly summarizes specifications of XRPIX8 relevant to this study. As noted

¹XRPIX8 has five subversions. “XRPIX8 with the optimized PDD

structure” here is specifically XRPIX8.5 in the terminology of [19].

in the previous section, the large sensor layer thickness is one of the most important features of XRPIX and is advantageous for X-ray detection in the higher energy band even above 10 keV. Since the pixel size is kept as small as possible for high spatial resolution, the thickness of the sensor layer is large relative to the pixel size in comparison with other X-ray silicon pixel detectors. We apply a high back bias voltage of -300 V to the sensor layer in order to suppress the overspreading of charge cloud and make conventional grade selection applicable [20]. The remaining description in this section focuses on the pixel circuit and the format of data, which are related to the following post-DAQ processing and spectroscopic performance study.

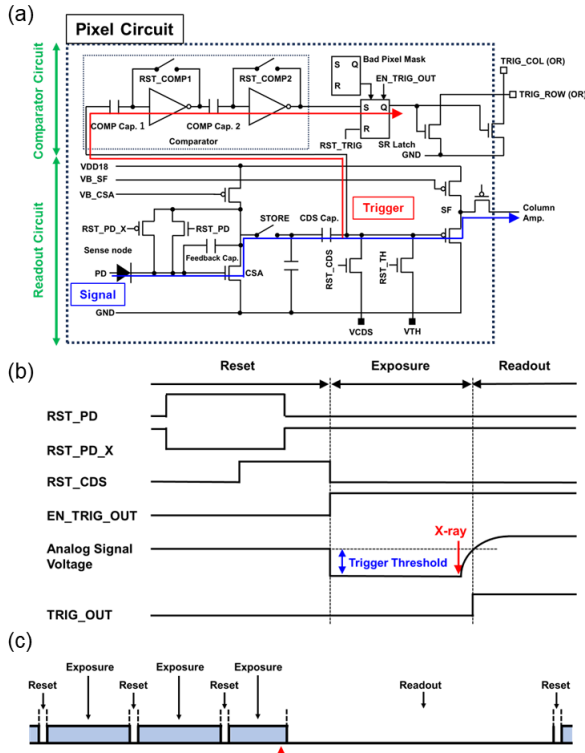


Fig. 1: (a) Pixel circuit of XRPIX8. (b) Timing diagram of the operation. (c) A part of the time sequence of operation. The blue periods correspond to live time periods.

Fig. 1 (a) shows the pixel circuit of XRPIX8. The pixel circuit consists of a readout circuit and a comparator circuit. The readout circuit includes a charge-sensitive amplifier (CSA) circuit to convert the charge produced by an X-ray photon to a signal voltage and a correlated double sampling (CDS) circuit to suppress the kT/C reset noise in the sense node. The comparator circuit is for trigger output.

Fig. 1 (b) shows the timing diagram of the operation. Readout circuits are reset by RST_PD, RST_PD_X and RST_CDS. An exposure starts when RST_CDS is turned off and EN_TRIG_OUT is turned on. EN_TRIG_OUT makes comparator circuits ready to output a digital trigger signal, TRIG_OUT. Charge accumulation from the sense node starts at this point. When the signal voltage exceeds the trigger threshold at a certain pixel, TRIG_OUT is output from the comparator circuit of the pixel. An exposure time is defined as the time from when the RST_CDS is turned off until the digital trigger signal is output, and hence each event has a different exposure time. A more detailed timing diagram for the pixel circuit and description are given in [17].

Fig. 1 (c) shows a part of the time sequence of operation. We reset all the pixel circuits every $100 \mu\text{s}$ unless an X-ray is detected and a digital trigger signal is output during the period. It takes $\sim 30 \mu\text{s}$ to reset. The period of $100 \mu\text{s}$ can be modified according to an observation purpose. When the digital trigger signal is output due to incident X-ray, the analog signal voltages of 8×8 pixels centered on the triggering pixel are read out and stored as an event. It takes $\sim 310 \mu\text{s}$ to readout. Therefore, the live time fraction of an observation depends on its incident X-ray count rate.

If the readout size is restricted to be smaller than the 8×8 pixel region, the readout time will be correspondingly shorter. However, the readout size should be sufficiently larger than the charge cloud sizes and should be processed with 2^n from a design perspective. The 8×8 pixel region is the smallest size that satisfies the above.

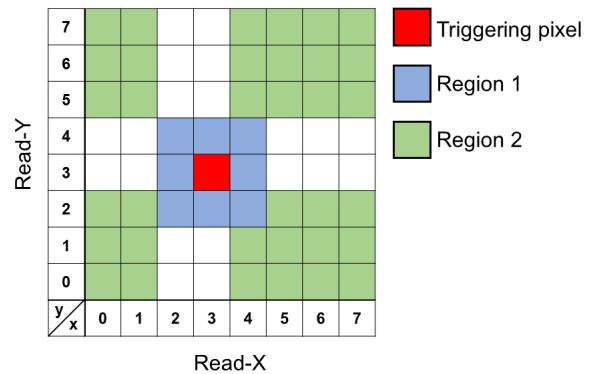


Fig. 2: 8×8 pixel map of an event in the relative coordinate.

Two coordinate systems are used here. One is the absolute coordinate to give the position in the 96×96 pixels, in which “column address” and “row address” are used to express horizontal and vertical axes, respec-

tively. The other is the relative coordinate to give the position in the analog-signal-readout 8×8 pixels, in which “read-X” and “read-Y” are used to express horizontal and vertical axes, respectively. Fig. 2 shows the pixel map of an event in the relative coordinate. The triggering pixel is placed at (read-X, read-Y) = (3, 3). Charge sharing due to the charge diffusion during the drift in the sensor layer commonly occurs in silicon pixel sensors. The surrounding 8 pixels, labeled as region 1, could have the signal charge by the charge sharing considering the pixel and charge cloud sizes [20]. Columns at read-X = 2, 3 and rows at read-Y = 3, 4 can be affected by the trigger function interference (see next section). Outer pixels, labeled as region 2, are not expected to share the signal charge nor to be affected by the trigger function interference. The analog signal voltages of 64 pixels are digitized by an analog-to-digital converter and stored as raw values. The unit of the raw value is analog to digital units (ADU), which represents the digitized analog signal voltage, and 1 ADU is 488 μ V.

3. Experiments and data processing

In this experiment, XRPIX8 was irradiated from the back side with X-rays/ γ -rays from the radioisotopes, ^{57}Co and ^{241}Am , and an X-ray tube with a Ti target. A back bias voltage of -300 V was applied to fully deplete the sensor layer. We acquired two data sets, “evaluation data” and “calibration data”. The evaluation data is the subject of this spectroscopic performance study, and final numbers are deduced from the evaluation data. If the evaluation data is calibrated with themselves, the results would be biased to be better than they actually are. Therefore, we derived the calibration parameters from the calibration data and then calibrated the evaluation data with them in the gain correction and energy calibration (step 4 and 5 in the following). The evaluation data was taken from the 8×8 pixel region with the column addresses of 17–24 and the row addresses of 20–27. The calibration data was taken from the 16×16 pixel region centered on the 8×8 pixel region. This is because an event whose triggering pixel is located at the outer pixels of the 8×8 pixel region has information of pixels outside that region.

Fig. 3 shows a flowchart of post DAQ processing. There are five steps in creating X-ray spectra from raw X-ray events. From step 1 to step 3, the same data processing applies to both calibration and evaluation data independently. From step 4 to step 5, parameters derived from the calibration data are used to calibrate the evaluation data. The details of each step are described in the following. The data used in the figures shown in the

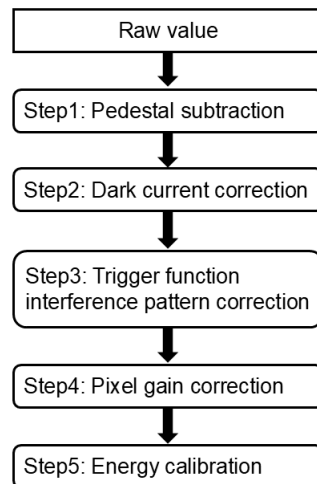


Fig. 3: Flowchart of post DAQ processing.

following subsections are the evaluation data otherwise noted.

Step 1: Pedestal subtraction

Each pixel has a different pedestal value in the absolute coordinate. Fig. 4 illustrates the calculation procedure of the pedestal value of a given pixel. All events containing that pixel in the region 2 of the relative coordinate are extracted, and the average of the raw values of that pixel in such events is calculated and used as the pedestal value of that pixel. The pedestal value for each single pixel is calculated in this way. Fig. 5 shows the resulting pedestal value map. The pedestal values are calculated for the pixels outside the 8×8 region because they could be in the region 1 of the relative coordinate due to the charge sharing. We subtract the pedestal value from the raw value for each pixel, and the raw value minus the pedestal value is recorded as the pulse height.

Step 2: Dark current correction

Fig. 6 left shows the pulse height in the region 2 as a function of the exposure time. It is clear that the pulse height correlates with the exposure time due to larger contributions of dark current in longer exposure time events. Assuming that the dark current is constant, the pulse height should increase linearly as a function of exposure time. This actually applies after 20 μ s, but does not before 20 μ s. The detailed mechanism is currently unknown and we empirically approximate the relation with a fourth-order polynomial function. We then add a correction to the pulse height pixel by pixel and event by event using the polynomial function. Fig. 6 right

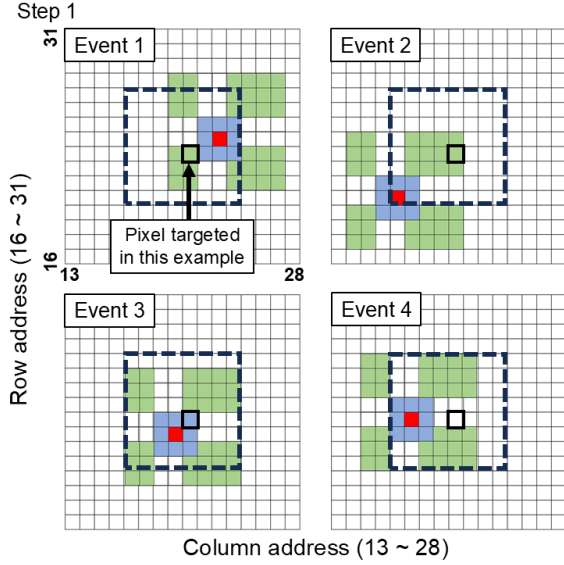


Fig. 4: Illustration of the pedestal calculation of a given pixel, which is edged with a black solid line in this figure. The black dashed line indicates the 8×8 region where the spectroscopic performance is investigated. The pixel targeted in this example is contained in the region 2 of the relative coordinate in the cases of event 1 and event 2, but not in the cases of event 3 and event 4. In this example, the raw values of that pixel in the event 1 and event 2 are used for the pedestal calculation of that pixel.

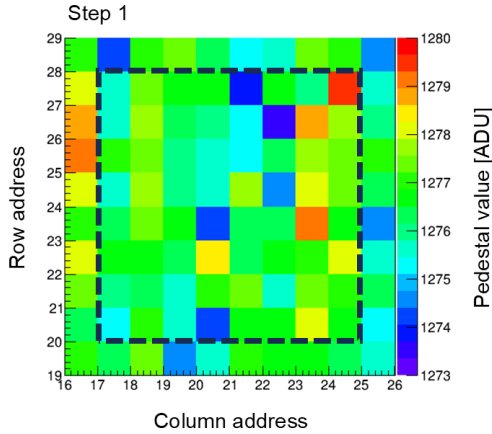


Fig. 5: Pedestal value map of the 10×10 pixels. The black dashed line indicates the 8×8 region where the spectroscopic performance is investigated

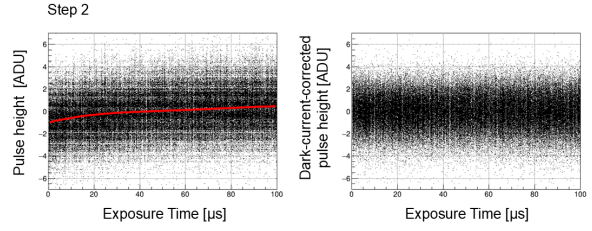


Fig. 6: Pulse height (left) and dark-current-corrected pulse height (right) as a function of the exposure time in the region 2. The red solid line in the left panel is the best fit curve with the fourth-order polynomial function.

shows the dark-current-corrected pulse height as a function of the exposure time. The dark-current-corrected pulse heights are apparently distributed around 0 ADU with no exposure time dependence, indicating that the dark current contribution is successfully eliminated.

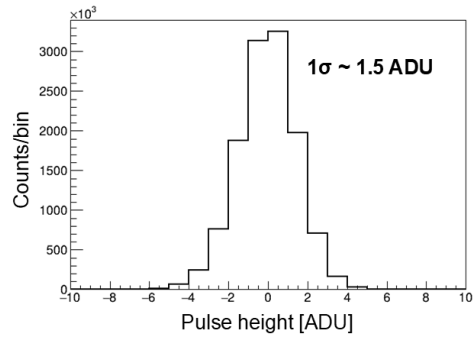


Fig. 7: Pulse height distribution in the region 2 of the relative coordinate after the dark current correction.

Fig. 7 shows the pulse height distribution in the region 2 after the dark current correction. This plot is a projection of Fig. 6 right onto the y axis. We hereafter call this pulse height distribution as the zero-peak spectrum.

Step 3: Trigger function interference pattern correction

Fig. 8 left shows a map of the mean pulse height after step 2 of the events with a single trigger signal output in the relative coordinate. A characteristic pattern appears at the column at read-X = 3 and the row at read-Y = 4. In order to measure the pulse height difference in the characteristic pattern lines, we define the column at read-X = 1 and the row at read-Y = 5 as reference lines. The differences in pulse height compared to the reference lines are $+1.8 \pm 0.1$ ADU and -3.3 ± 0.1 ADU in the column of read-X = 3 and the row of read-Y = 4, respectively, except for the pixels in the region 1 and triggering pixel in the relative coordinate. As shown in

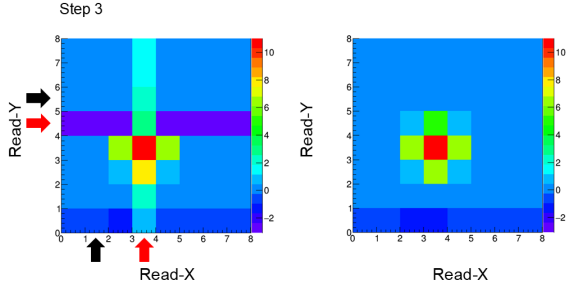


Fig. 8: Map of the mean pulse height after step 2 of the event with a single trigger signal output in the relative coordinate before (left) and after (right) trigger function interference pattern correction. The characteristic pattern and the reference lines are indicated by red and black arrows in the left panel, respectively.

Fig. 8 right, the characteristic pattern disappears by subtracting 1.8 ADU from the pulse heights of the pixels at read-X = 3 and adding 3.3 ADU to the pulse heights of the pixels at read-Y = 4. In doing so, the pulse height of the pixel at (read-X, read-Y) = (3, 4), where the characteristic pattern lines overlap, is added by 1.5 ADU. After the correction, the pulse height distribution around the triggering pixel becomes more symmetric as expected.

Regardless of whether the signal charge is read out or not, when the comparator circuit operates, this characteristic pattern always appears. We confirmed it in the following two experiments. In the first experiment, we fixed the central pixel coordinate of the 8×8 pixels readout region at (X, Y) and opened the trigger mask² only at (X, Y+20). In this case, only the pixel at (X, Y+20) could send out a digital trigger signal, and due to the trigger, the 8×8 pixels centered at (X, Y) were read out without no signal charge because no X-ray photon came in the 8×8 pixels. In this experiment, the characteristic pattern appeared at the column of read-X = 3, but did not appear at the row of read-Y = 4. When we opened the trigger mask only at (X+20, Y), the characteristic pattern appeared at the row of read-Y = 4, but did not appear at the column of read-X = 3. In the second experiment, we used a non-triggered frame mode, in which all pixels are read out serially without using the trigger function [21]. Even in this mode, the comparator circuit operates regardless of the pixel readout sequence. We took two data sets with trigger thresholds of 20 mV and 500 mV. The former is the same as that of the event-driven readout mode, and the latter is way above signal voltages produced by incident X-rays used in this experiment. The characteristic pattern appeared

²The trigger mask is a function that prevents the specified pixel from sending out a digital trigger signal.

in the data taken with the trigger threshold of 20 mV, but not with 500 mV. In addition to these experiments, we also note that the offset of the characteristic pattern was constant regardless of incident X-ray energy.

The characteristic pattern is likely due to interference between the digital trigger lines and the sense node/the CSA circuit as the digital trigger lines run through pixels vertically and horizontally. However, the mechanisms of why the horizontal characteristic pattern appears one row above the triggering pixel and why the offsets in pulse height have reverses in the vertical and horizontal characteristic lines are currently unknown.

An event could have multiple trigger signals because the signal voltage of the charge-sharing pixel sometimes exceed the trigger threshold. In this case, the 8×8 pixels centered on the triggering pixel with the larger column and row addresses are read out, and other triggering pixels are consequently placed at (read-X, read-Y) = (2, 2) and/or (2, 3) and/or (3, 2). Then the characteristic pattern can also appear at the column of read-X = 2 and/or the row of read-Y = 3 due to the non-centered triggering pixels. The correction is made depending on the number and position of the triggering pixels.

Step 4: Pixel gain correction

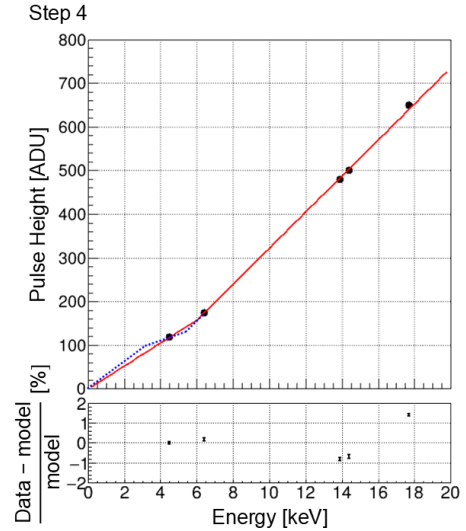


Fig. 9: Center value in pulse height of major emission line as a function of energy in a specific pixel, which is made from the single-pixel event spectrum of the calibration data. The red solid line is the best fit gain curve. The blue dotted line below 6.4 keV is the putative gain curve discussed in step 5. The plot below shows the residuals between the data points and the best fit gain curve as a percentage.

We define a split threshold to judge how the charge-sharing occurs in an event. If the pulse height af-

ter step 3 of a surrounding pixel in the region 1 exceeds the split threshold, we acknowledge that the surrounding pixel contains signal charge. Considering the charge cloud and pixel sizes, the charge-sharing can occur within 4 pixels at the most including the triggering pixel [20]. We then sort all the events into single-pixel events, double-pixel events, triple-pixel events and quadruple-pixel events depending on the number of pixels having signal charge. The split threshold is set to be 3 times the standard deviation of the zero-peak spectrum (Fig. 7).

With the calibration data, we first make single-pixel event spectra pixel by pixel and measured center values of major X-ray/ γ -ray emission lines in pulse height. Fig. 9 shows the center value in pulse height of major emission line as a function of X-ray energy measured in a specific pixel. The data points at 6.4 and 14.4 keV and those at 13.9 and 17.7 keV come from the ^{57}Co and ^{241}Am spectra, respectively. The data point at 4.5 keV is obtained from the X-ray tube spectrum with a Ti target. These data points do not appear to follow a straight line through the origin: the slope appear to be steeper in the higher energy side.

We here adopt a broken line model to fit the data points. A red solid line in Fig. 9 represents the best fit gain curve in this example. In such a way, a gain curve is determined for each 8×8 pixels with the calibration data, and the individual pulse heights of the evaluation data are calibrated with the gain curve. The energy of an event is calculated by summing up the calibrated pulse height of the triggering pixel and those of its surrounding pixels above the split threshold.

Although we did not obtain X-ray data below 4.5 keV, we realized that the linearity between the energy and the pulse height was not maintained in the low energy side by analyzing double-pixel event data. Since double-pixel events share the signal charge with two pixels, the charge-sharing pixel can have small charge that is equivalent to those low energy X-rays produce. Therefore, albeit indirectly, we can investigate the gain linearity in the low energy side using the double-pixel events. Fig. 10 (a) shows the 6.4 and 7.1 keV emission line spectra of the double-pixel events made with the evaluation data. It is obvious that the spectrum significantly varies depending on the pulse height ratio (PHR) of the adjacent charge-sharing pixel to that of the triggering pixel. Fig. 10 (b) shows the center values of 6.4 and 7.1 keV emission lines as a function of PHR. As the PHR increases, the center value of emission line shifts first to the lower energy side and then to the higher energy side. If the gain linearity is maintained in the low energy side, neither the spectral shape nor the center

value changes regardless of the value of the PHR. This indicates that the linear relationship does not hold in the low energy side. We refrain from introducing a further complex modification to the broken line model without a physical basis and leave these distortions as systematic uncertainties.

Fig. 11 shows the histogram of the output gain value in the high energy side of the broken line model measured with the calibration data. The output gain is calculated from the slope of the high energy side of the broken line model using $1 \text{ ADU} = 488 \mu\text{V}$, instrumentation amplifier gain on our evaluation board of 2.0, and a mean ionization energy in silicon of 3.65 eV [22]. The central value is comparable with that of our study with previous XRPIX [23]. The pixel-to-pixel gain variation is 1.2 % in standard deviation, which is slightly larger than 0.9 % obtained in our previous study [24].

Step 5: Energy calibration

Fig. 12 left shows the single-, double-, triple- and quadruple-pixel event spectra from ^{57}Co and ^{241}Am after step 4. In spite of the gain correction in step 4, the center energies of emission lines in the single-, double-, triple-, and quadruple-pixel events spectra are getting higher in this order. This systematic shift could happen if undetected charge below the split threshold is significant. Single-pixel events have the highest chance to be affected by this effect, and double-, triple-, quadruple-events have lower chance in this order. In order to test this effect, we made the spectra summing up pulse heights of the 3×3 pixel centered on the triggering pixel and found that systematic shift shown in Fig. 12 left barely change. Then, this systematic shift may suggest that approximating the gain curve with a broken line model is too simplistic. Larger charge-sharing events tend to have more signal pixels whose pulse height comes to the low energy side. Therefore, this result indicates that the conversion ratio from ADU to energy in the low energy side is too high. In other words, the slope of the broken line model in the low energy side in Fig. 9 is too low, requiring another break point for the model. The putative gain curve discussed here is also shown in Fig. 9. This winding gain curve is also suggested to some extent by the behavior shown in Fig. 10.

We re-calibrate the energy scale for each event pattern with the calibration data spectra corresponding to Fig. 12 left and then apply the derived energy scale to the evaluation data spectra. Fig. 12 right shows the spectra after the final energy calibration, in which the systematic shift of the center energies disappears.

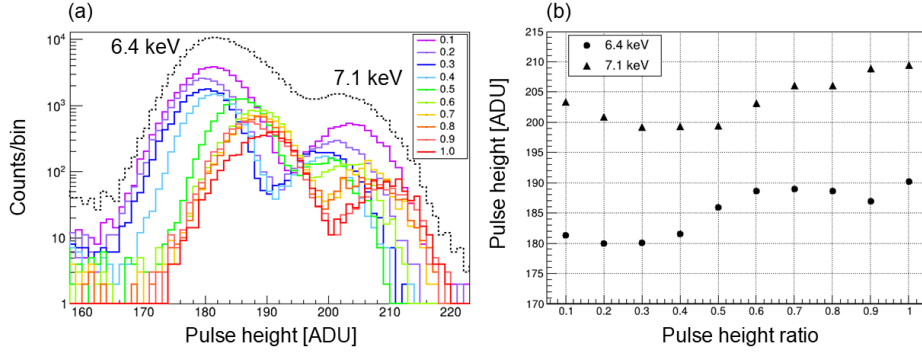


Fig. 10: (a) 6.4 and 7.1 keV emission line spectra of the double-pixel events. The black-dotted-line spectrum is made with all the double-pixel events. The solid-line spectra are made by dividing the events according to the pulse height ratio of the pulse height of the adjacent charge-sharing pixel to that of the triggering pixel. The pulse height ratio becomes larger from cold to hot colors from 0.1 to 1.0. (b) The center values of 6.4 and 7.1 keV emission lines as a function of the pulse height ratio.

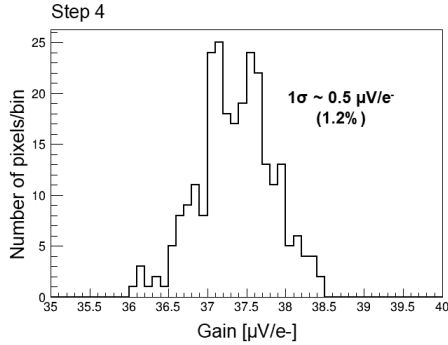


Fig. 11: Histogram of the output gain value in the high energy side of the broken line model.

4. Spectroscopic performance

Fig. 13 shows ^{57}Co and ^{241}Am spectra of the single-pixel events and all-pixel events obtained with XRPIX8 with the optimized PDD structure. All-pixel events include the single-, double-, triple- and quadruple-pixel events, and the all-pixel event spectrum is simply the sum of the spectra shown in Fig. 12 right. The energy resolutions at 6.4 and 13.9 keV are summarized in Table 3. The energy resolution at 6.4 keV of the single-pixel event spectrum is 178 ± 1 eV in full width at half maximum (FWHM), which is the best value ever obtained in our history of the XRPIX development and comparable to that of CCDs used in the XRISM observatory [25]. On the other hand, the energy resolution at 6.4 keV of the all-pixel event spectrum is 291 ± 1 eV in FWHM, which is not as good as that of CCD. Quantitative evaluation of the degradation from the single-pixel event spectrum to the all-pixel event spectrum will be given in section 5.

5. Discussion

Thanks to the optimized PDD structure and the refined data calibration, we achieved the best spectroscopic performance in our development history. However, there is still room for improvement in the spectroscopic performance of XRPIX. Fig. 10 exhibits a clear deviation from the linear relationship between the energy and the pulse height in the low energy side, which is a serious drawback of the current XRPIX. We consider that the gain non-linearity in the low energy side comes from excessive charge injection to the CSA circuit in Fig. 1.

The CSA circuit is reset by turning on the CMOS switch that is shown as a pair of RST_PD (NMOS) and RST_PD_X (PMOS) in Fig. 1, and then charge injection into the CSA circuit occurs at the time when the CMOS switch is turned off, namely the start of exposure. The amount of the charge injection is determined by the design of the CMOS switch. Because the thick depletion layer is one of the main characteristics of XRPIX, the circuitry design was aimed for a wide dynamic range covering the higher energy band up to several tens of keV. To this end, based on a circuit simulation, the size of the PMOS transistor is designed to be significantly larger than that of the NMOS transistor so that a large number of holes, the opposite of electrons in the signal charge, are injected to CSA. Actually, XRPIX8 has the wide dynamic range and the good linearity in the high energy side in the evaluation of the single-pixel events. On the other hand, due to excessive charge injection, the low energy side is considered to have fallen outside the linear region. The circuit simulation with an excessive charge injection actually reproduced that the gain in the low energy side becomes low compared to that in

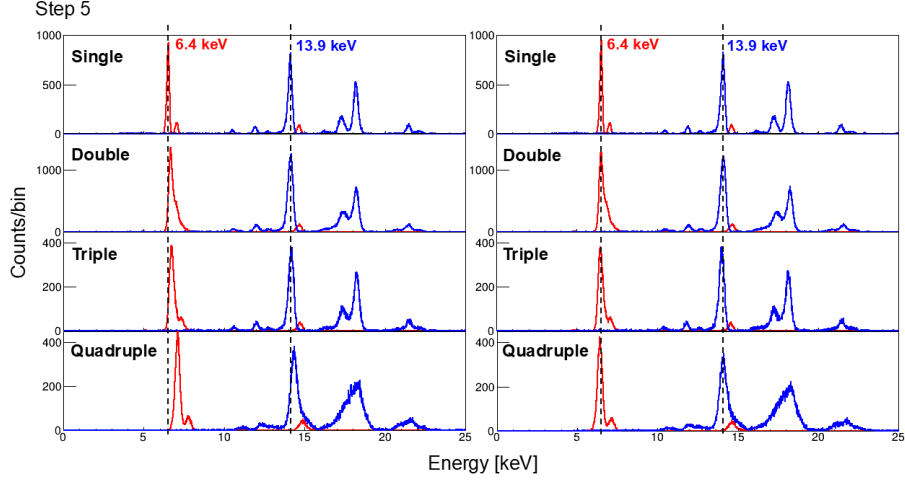


Fig. 12: Single-, double-, triple- and quadruple-pixel event spectra before (left) and after (right) energy calibration. ^{57}Co and ^{241}Am spectra are shown in red and blue colors, respectively. The black dashed lines denote the emission line center of 6.4 keV and 13.9 keV in the spectra of the single-pixel events for eye guide.

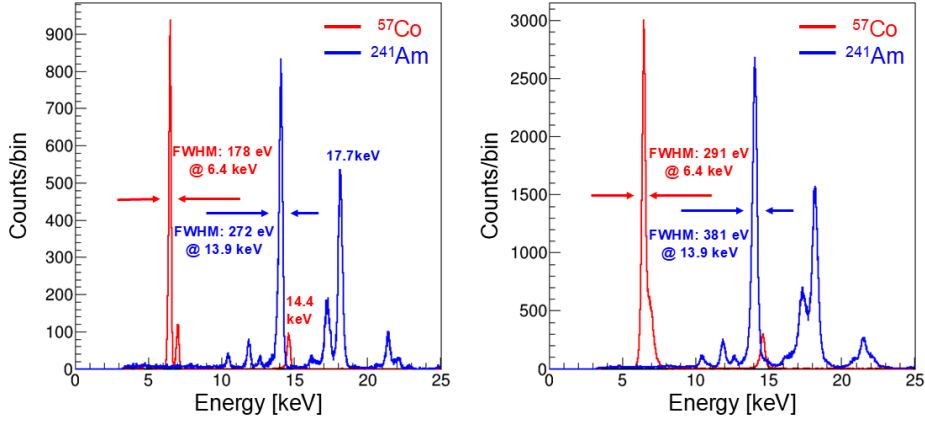


Fig. 13: ^{57}Co (red) and ^{241}Am (blue) spectra of the single-pixel events (left) and all-pixel events (right) obtained with XRPIX8 with the optimized PDD structure.

Table 3: Energy resolution.

Event pattern	6.4 keV (FWHM) [eV]	13.9 keV (FWHM) [eV]
Single	178 ± 1	272 ± 2
All	291 ± 1	381 ± 2

the high energy side as we experienced. Optimization of the amount of the charge injection is our next step to resolve the gain non-linearity in the low energy side and to further improve the spectroscopic performance of XRPIX.

The energy resolution in FWHM (ΔE) is in general

expressed as

$$\Delta E = 2\sqrt{2 \ln 2} W \sqrt{\frac{E}{W} F + n^* (\sigma_R^2 + \sigma_D^2) + \left(\frac{E}{W} \sigma_{\text{gain}}\right)^2}, \quad (1)$$

where E , W , F , n^* , $\sqrt{(\sigma_R^2 + \sigma_D^2)}$ and σ_{gain} are the incident X-ray energy, mean ionization energy in silicon of 3.65 eV, Fano factor of 0.128 [26], effective number of pixels involved in the calculation of the energy, energy-independent noise per pixel, and pixel gain variation, respectively [24]. The first term in the square root is the Fano noise. σ_R and σ_D in the second term are the readout noise of the XRPIX electronics and dark current noise. Assuming that these noises operate independently pixel by pixel, the contribution of the collective

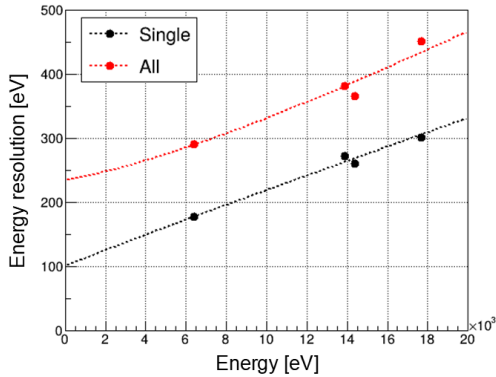


Fig. 14: Energy resolution as a function of energy measured from the single-pixel event spectrum (black) and all-pixel event spectrum (red). The dashed lines are the best fit curves with Eq. 1.

Table 4: Best-fit parameters of $\sqrt{(\sigma_R^2 + \sigma_D^2)}$ and σ_{gain} with Eq. 1.

Event pattern	$\sqrt{(\sigma_R^2 + \sigma_D^2)}$ [e ⁻]	σ_{gain} [%]
Single	11.8	0.5
All	18.8	0.7

noise per pixel is multiplied by n^* . In the case of the single-pixel event spectrum, n^* is unity by definition. Whereas, in the case of the all-pixel event spectrum, n^* depends on E because the charge cloud size depends on E [20]. We measured the number ratio of each event pattern using major emission lines in the all-pixel event spectrum and estimated the energy dependency of n^* . Then, we derived an empirical relation between n^* and E as $n^* = 0.9 \times 10^{-5}E + 2.1$, where E is in the unit of eV. The third term in the square root would be ideally zero because we corrected the pixel gain variation, but realistically has a certain value due to imperfection of our correction.

Fig. 14 plots ΔE as a function of energy measured from the single-pixel event spectrum and all-pixel event spectrum. Well-isolated emission lines at 6.4, 13.9, 14.4 and 17.7 keV were selected in this evaluation. The best fit curves with Eq. 1 are also shown and parameters obtained are summarized in Table 4. The values of $\sqrt{(\sigma_R^2 + \sigma_D^2)}$ are obtained as 11.8 e⁻ and 18.8 e⁻ from the single- and all-pixel event spectra, respectively. The former is fully consistent with the value from our previous study, in which single-pixel events from one specific pixel were used [19]. The latter is significantly larger than the former. The cause of this degradation in the all-pixel event spectrum is likely the gain non-linearity in the low energy side. Even limiting the evaluation energy to the high energy side, the multi-pixel

event spectrum becomes distorted if the gain linearity was not maintained in the low energy side because the pulse heights of charge-sharing pixels could be effectively in the range of the low energy side. This effect makes the line shape asymmetric, having non-Gaussian tails in the high and/or low energy side as is seen in Fig. 10 left.

The values of σ_{gain} are obtained as 0.5% and 0.7% from the single- and all-pixel event spectra, respectively. Both values are lower than the original value of 1.2% in Fig. 11, indicating that the pixel gain correction certainly works, but not enough to eliminate all the variation. Especially, the larger σ_{gain} of the all-pixel event spectrum suggests that degree of inaccuracy in the pixel gain correction is greater in the low energy side.

6. Summary

We have presented a detailed study of the X-ray spectroscopic performance of XRPIX8 with the optimized PDD structure. The study is performed on the event-driven readout mode data taken with operation temperatures of -60 °C. The details of the post-DAQ processing are also presented. The energy resolutions in FWHM at 6.4 keV of the single-pixel and all-pixel event spectra are 178 ± 1 eV and 291 ± 1 eV, respectively. These are the best records in our XRPIX series. We have discussed that the current spectroscopic performance is mainly limited by the gain non-linearity in the low energy side due to excessive charge injection to the CSA circuit. Optimization of the amount of the charge injection is expected to further improve the spectroscopic performance of XRPIX, especially for the all-pixel event spectrum.

7. Acknowledgments

We acknowledge the valuable advice and the manufactures of XRPIXs by the personnel of LAPIS Semiconductor Co., Ltd. This study was supported by JSPS KAKENHI Grant Numbers 21H01095, 23K20850 and by JST SPRING, Grant Number JPMJSP2105. This study was also supported by the VLSI Design and Education Center (VDEC), the University of Tokyo in collaboration with Cadence Design Systems, Inc., and Mentor Graphics, Inc.

References

- [1] M. Bigas, et al., Review of cmos image sensors, *Microelectronics Journal* 37 (5) (2006) 433–451.

- [2] M. R. Alarcon, et al., Scientific cmos sensors in astronomy: Imx455 and imx411, *Publications of the Astronomical Society of the Pacific* 135 (1047) (2023) 055001.
- [3] B. E. Burke, et al., Ccd soft x-ray imaging spectrometer for the asca satellite, *IEEE Transactions on Nuclear Science* 41 (1) (1994) 375–385.
- [4] G. P. Garmire, et al., Advanced ccd imaging spectrometer (acis) instrument on the chandra x-ray observatory, in: *Proceedings of SPIE* 4851 (2003) 28–44.
- [5] M. J. L. Turner, et al., The european photon imaging camera on xmm-newton: The mos cameras, *Astronomy and Astrophysics* 365 (1) (2001) L27–L35.
- [6] K. Koyama, et al., X-ray imaging spectrometer (xis) on board suzaku, *Publications of the Astronomical Society of Japan* 59 (2007) S23–S33.
- [7] P. Predehl, et al., The erosita x-ray telescope on srg, *Astron. Astrophys.* 647 (2021) A1.
- [8] T. Tanaka, et al., Soft x-ray imager aboard Hitomi (ASTRO-H), *Journal of Astronomical Telescopes, Instruments, and Systems* 4 (1) (2018).
- [9] H. Nakajima, et al., In-orbit performance of the soft x-ray imaging system aboard hitomi (astro-h), *Publications of the Astronomical Society of Japan* 70 (2) (2018) 21.
- [10] K. Mori, et al., Status of xtend telescope onboard x-ray imaging and spectroscopy mission (xrism), in: *Proceedings of SPIE* 13093 (2024) 130931I.
- [11] M. Bautz, et al., Fast, low-noise image sensor technology for strategic x-ray astrophysics missions, in: *Proceedings of SPIE* 13093 (2024) 130931Q.
- [12] N. Meidinger, et al., erosita camera array on the srg satellite, *Journal of Astronomical Telescopes, Instruments, and Systems* 7 (2) (2021) 025004.
- [13] E. D. Miller, et al., The high-speed x-ray camera on axis, in: *UV, X-Ray, and Gamma-Ray Space Instrumentation for Astronomy XXIII*, Vol. 12678, SPIE, 2023, p. 1267816.
- [14] W. Q. et al., Improving the x-ray energy resolution of a scientific cmos detector by pixel-level gain correction, *Publications of the Astronomical Society of the Pacific* 135 (1044) (2023) 025003.
- [15] T. G. Tsuru, H. Hayashi, K. Tachibana, et al., Kyoto’s event-driven x-ray astronomy soi pixel sensor for the force mission, in: *Proceedings of SPIE* 10709 (2018).
- [16] Y. Arai, T. Miyoshi, Y. Unno, et al., Development of SOI pixel process technology, *Nuclear Instruments and Methods in Physics Research Section A: Accelerators, Spectrometers, Detectors and Associated Equipment* 636 (2011) S31–S36.
- [17] A. Takeda, Y. Arai, S. G. Ryu, et al., Design and evaluation of an soi pixel sensor for trigger-driven x-ray readout, *IEEE Transactions on Nuclear Science* 60 (2) (2013) 586–591.
- [18] H. Kamehama, S. Kawahito, S. Shrestha, et al., A low-noise x-ray astronomical silicon-on-insulator pixel detector using a pinned depleted diode structure, *Sensors* 18 (1) (2018) 27.
- [19] M. Yukumoto, K. Mori, A. Takeda, et al., Design study and spectroscopic performance of soi pixel detector with a pinned depleted diode structure for x-ray astronomy, *Nuclear Instruments and Methods in Physics Research Section A: Accelerators, Spectrometers, Detectors and Associated Equipment* 1060 (2024) 169033.
- [20] K. Hagino, K. Oono, K. Negishi, et al., Measurement of charge cloud size in x-ray soi pixel sensors, *IEEE Transactions on Nuclear Science* 66 (7) (2019) 1897–1905.
- [21] S. G. Ryu, T. G. Tsuru, S. Nakashima, et al., First performance evaluation of an x-ray soi pixel sensor for imaging spectroscopy and intra-pixel trigger, *IEEE Transactions on Nuclear Science* 58 (5) (2011) 2528–2536.
- [22] J. R. Janesick, *Scientific Charge-Coupled Devices*, SPIE, 2001.
- [23] S. Harada, T. G. Tsuru, T. Tanaka, et al., Performance of the silicon-on-insulator pixel sensor for x-ray astronomy, xrpix6e, equipped with pinned depleted diode structure, *Nuclear Instruments and Methods in Physics Research Section A: Accelerators, Spectrometers, Detectors and Associated Equipment* 924 (2019) 468–472.
- [24] R. Kodama, T. G. Tsuru, T. Tanaka, et al., Low-energy x-ray performance of SOI pixel sensors for astronomy, "XRPIX", *Nuclear Instruments and Methods in Physics Research Section A: Accelerators, Spectrometers, Detectors and Associated Equipment* 986 (2021) 164745.
- [25] K. Mori, et al., Xtend, the soft x-ray imaging telescope for the x-ray imaging and spectroscopy mission (xrism), in: *Proceedings of SPIE* 12181 (2022).
- [26] I. V. Kotov, et al., Pair creation energy and fano factor of silicon measured at 185 k using x-rays, *Nuclear Instruments and Methods in Physics Research Section A: Accelerators, Spectrometers, Detectors and Associated Equipment* 901 (2018) 126–132.